Heavy residues and intermediate-mass fragment production in dissipative ^{197}Au+ ^{86}Kr collisions at $E/A=35$ MeV

B. Djerroud,* D. K. Agnihotri, S. P. Baldwin, W. Skulski, J. Tõke, and W. U. Schröder
Department of Chemistry, University of Rochester, Rochester, New York 14627

R. J. Charity, J. F. Dempsey, D. G. Sarantites, and L. G. Sobotka
Department of Chemistry, Washington University, St. Louis, Missouri 63130

B. Lott
Laboratoire National GANIL, BP 5027, Caen F-14021, France

W. Loveland
Oregon State University, Corvallis, Oregon 97331

K. Aleklett
Uppsala University, S-611 82 Nyköping, Sweden
(Received 11 August 2000; published 6 August 2001)

Neutrons and charged light and intermediate-mass products from the ^{197}Au+ ^{86}Kr reaction at $E_{lab}/A=35$ MeV were measured with 4π angular coverage, in coincidence with projectilelike (PLFs) and targetlike fragments (TLFs). The characteristics of PLF and TLF yields and their correlation with neutron, light-charged particles, and intermediate-mass fragments (IMFs) are consistent with a scenario where essentially all collisions proceed through a dissipative stage. It is found that the damping of the available kinetic energy into thermal excitation is essentially incomplete, with no positive evidence for complete damping. Slow, massive reaction products are observed with significant yields. These products, termed also heavy residues, are identified as TLF evaporation residues and as TLF fission fragments. The TLF fission mode is seen to fade away in favor of TLF evaporation residue production for excitation energies above 3–4 MeV/nucleon. The suppression of the TLF fission can be traced to the dynamical IMF production process which reduces considerably the sizes of the primary reaction fragments and, hence, their fissility.

DOI: 10.1103/PhysRevC.64.034603 PACS number(s): 25.70.Lm, 25.70.Mn, 25.70.Pq

I. INTRODUCTION

The study of reactions between heavy nuclei at Fermi energies ($E/A=20-100$ MeV) has attracted considerable experimental and theoretical interest. Among other things, this energy domain offers ample opportunities to study the mechanisms of the production of highly excited nuclear systems and the various modes of their subsequent disintegration. One of the phenomena that has attracted significant interest is the disappearance of the fission mode with increasing bombarding energies [1] and the observation of an increasing cross section for very slow ($E/A \sim 0.1-0.5$ MeV) heavy residues (HRs), with masses comparable to the mass of the target, in radiochemical studies [2,4]. In spite of their large production cross sections, the presence of such residues has been overlooked in many experiments because of their low energies. Because of the large reaction cross section, increasing with increasing beam energy, HR production clearly constitutes an important nuclear reaction mode that could possibly inhibit, via competition, the fission mode at sufficiently high excitation energies. The abundant production of heavy residues has been observed in collisions of various projectiles from C to Xe with heavy targets such as Au, Th, and U [2,4–9] and, consequently, a number of scenarios have been considered [2,4–10] to account for this production. For example, fusionlike reactions (complete and incomplete fusion), fast fission, fragmentation, dissipative collisions, retardation of the dynamical fission process, and even spallation were considered as factors playing a role in the survival of HRs. The proposed explanations do not, however, include the possible governing role of reaction dynamics, for which there is growing evidence [11–14].

The main goal of the present study is the investigation of the HR production mechanism and, in particular, its possible connection to the dynamical intermediate-mass fragment (IMF) production process. This study entails exclusive 4π measurement of neutrons, light-charged particles, and intermediate-mass products, in coincidence with projectilelike and targetlike fragments (PLFs and TLFs). The ^{197}Au + ^{86}Kr reaction at $E/A=35$ MeV was chosen because, for this system, information on HRs is available from radiochemical measurements [2] where the HRs were observed with several barns of cross section.

In Sec. II, the experimental procedures and data analysis are described. Experimental results are presented and discussed in Sec. III, followed by conclusions in Sec. IV. A partial account of the present work has been presented elsewhere [15,16].

*Present address: Department of Physics and Astronomy, McMaster University, Hamilton, Ontario, Canada L8S 4M1.

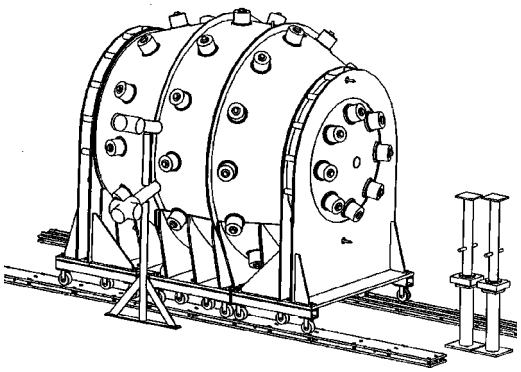

FIG. 1. Schematic view of the Rochester SuperBall neutron calorimeter.

II. EXPERIMENTAL PROCEDURES

The experiment was carried out at the National Superconducting Cyclotron Laboratory at Michigan State University. A beam of ^{86}Kr ions of $E_{lab}/A=35$ MeV from the K1200 cyclotron bombarded a 300 μg/cm^2 self-supporting ^{197}Au target, placed in the operational center of the detector setup. The setup included two 4π devices—the Rochester SuperBall neutron detector and the Washington University charged particle detector array Micro Ball—and thus provided an almost full 4π coverage for neutrons and charged products. The Micro Ball array was placed, along with heavy-residue and PLF detectors, inside the scattering chamber of the SuperBall, as seen in the schematic views of the SuperBall and of the experimental setup for charged products, Figs. 1 and 2, respectively.

Slow, massive reaction products were measured using

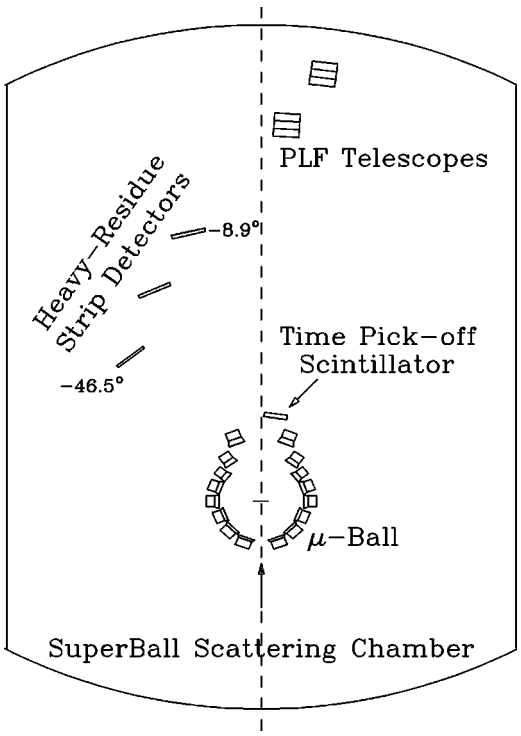

FIG. 2. Schematic view of the detector setup. See text.

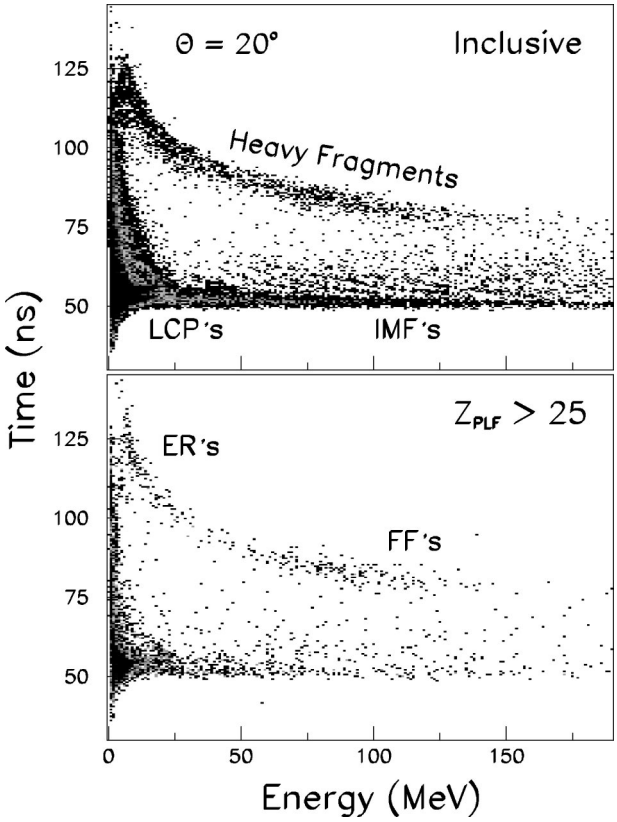

FIG. 3. Fragment identification plot as measured by a strip detector for all events (top) and for events with coincident projectilelike fragments with $Z_{PLF}>25$.

three multistrip silicon detectors covering the angular range from $-8.9°$ to $-46.5°$. Each detector had a thickness of 300 μm and an active area of 6.1×4.0 cm^2, divided into seven strips. In addition to the energy measurement, time-of-flight information was obtained using timing signals derived from either the accelerator *rf* signal or a 17-mg/cm^2-thick plastic scintillator detector placed at a small forward angle close to the target.

A typical fragment identification spectrum, as measured by a strip detector, is shown in the upper panel of Fig. 3 in the form of a scatter plot of time of flight versus energy. The achieved time resolution was sufficient to distinguish between light-charged particles, intermediate-mass fragments, and slow, heavy residues. The HRs are represented by the upper branch of events seen in this panel. An energy calibration of the multistrip detectors was achieved using α particles and fission fragments from a ^{252}Cf source. The energy of the products measured with the strip detectors was not corrected for pulse-height defect. However, based on the calibration measurement of ^{252}Cf fission fragments, this defect was estimated to be of the order of (24–36) MeV. Product identification was possible for HRs with apparent energies larger than 15 MeV.

Projectilelike fragments were measured with two multielement silicon detector telescopes placed on the side of the beam opposite to that of the HR detectors. These telescopes measured also IMFs. They covered an angular range from 1.9° to 9°, including the grazing angle at $\theta_{lab}^{gr}\sim6°$. Each

telescope consisted of three silicon detectors with thicknesses of 150, 480, and 3000 μm, respectively, and an active area of 2 cm$\times$2 cm, operated in ΔE-ΔE-E mode. Both telescopes allowed one to resolve atomic numbers in the range of $2 \leqslant Z \leqslant 38$. An energy calibration of the silicon detector telescopes was obtained using elastically scattered beam particles and the known maximum energy deposits in each detector by products with different atomic numbers. The fragment energy was calculated, with a relative resolution $<3\%$, by summing the energy deposits in all three constituent detectors of each telescope. In addition to charge and energy information, a two-dimensional position measurement was obtained from the position-sensitive elements of the telescopes, which had the architecture of a square matrix of 20$\times$20 discrete strips. It was found that the effective energy resolution in a second element of the telescope was adversely affected by the position dependence of the energy signal caused by variations in the thickness of the first element. Using data on elastically scattered projectiles, a two-dimensional energy correction matrix was constructed, which was subsequently used for an event-by-event energy calibration of the data.

Neutrons were detected using the Rochester SuperBall [17], a five-segment neutron calorimeter filled with 16-m^3 Gd-doped liquid scintillator (National Diagnostics ND-309). The five segments of the SuperBall represent five angular sectors with scintillator thicknesses between 1 m (at backward angles) and 1.5 m (at forward angles) and provide for a crude angular sensitivity of the device. The active volume of the device is viewed by a total of 52 Thorn-EMI 9390KB07 5 in. photomultipliers. A time reference signal for SuperBall event processing, indicating a reaction event in the target, was derived from the charged particle detectors. The SuperBall generates two types of signals in response to the neutrons penetrating its active volume. First, a prompt light signal is generated by the recoil protons during the initial neutron thermalization process. This signal provides a measure of the summed kinetic energy of all neutrons emitted in a reaction event, but contains also contributions by the reaction γ rays and by the energetic charged products of the neutron-induced reactions in the scintillator matter. Subsequently, the thermalized neutrons give rise to a series of delayed signals when they are captured one after another, randomly in time, by Gd nuclei within the active volume of the detector. These delayed signals are generated by the neutron capture γ rays. Their total number in an event is a good measure of the neutron multiplicity associated with this event, subject to a detection efficiency correction. The delayed signals were counted within a time interval of 64 μs following a reaction event in the target, which provides a good compromise for the conflicting requirements of the maximum detection efficiency, on the one hand, and the minimum background count rate, on the other hand.

The detection efficiency of the SuperBall was determined by simulating its response to neutrons under various neutron emission scenarios. For this purpose, a modified version [18] of the Monte Carlo code DENIS [19] was used, which modeled the history of an injected neutron as the latter interacts with the scintillator matter of known composition and geometry. The code considered the elastic, inelastic, and capture interactions of the neutron with the scintillator constituents. The efficiency was calculated as a function of the neutron energy and emission angle and tabulated for further use in the analysis of simulated reaction events. The angle-averaged capture efficiency is presented in the upper panel of Fig. 4 as a function of the neutron energy. As seen in this figure, for low and moderate neutron energies ($E_n < 15$ MeV), the efficiency is nearly constant and determined largely by the detection threshold E_{th} of the SuperBall for the light signals generated by the capture γ rays. The efficiency then decreases noticeably when neutron energies increase to 20 MeV and higher. At any rate, the efficiency for detecting for a neutron at least one interaction within the active volume of the SuperBall is nearly 100%, for the neutron energy spectrum of interest here. The dependence of the SuperBall detection efficiency on the reaction observables, such as the total kinetic-energy loss (TKEL) and/or impact parameter, was determined using the simulated events, describing the damped reaction scenario for the ^{197}Au+ ^{86}Kr system at $E/A = 35$ MeV. In this scenario, it is assumed that neutrons, as well as charged particles, are emitted sequentially from exited projectilelike and targetlike fragments produced in the course of a primary dissipative collision. The resulting neutron detection efficiency is presented in the lower panel of Fig. 4, as a function of the total kinetic-energy loss, assumed to be equal to the summed thermal excitation energy of PLFs

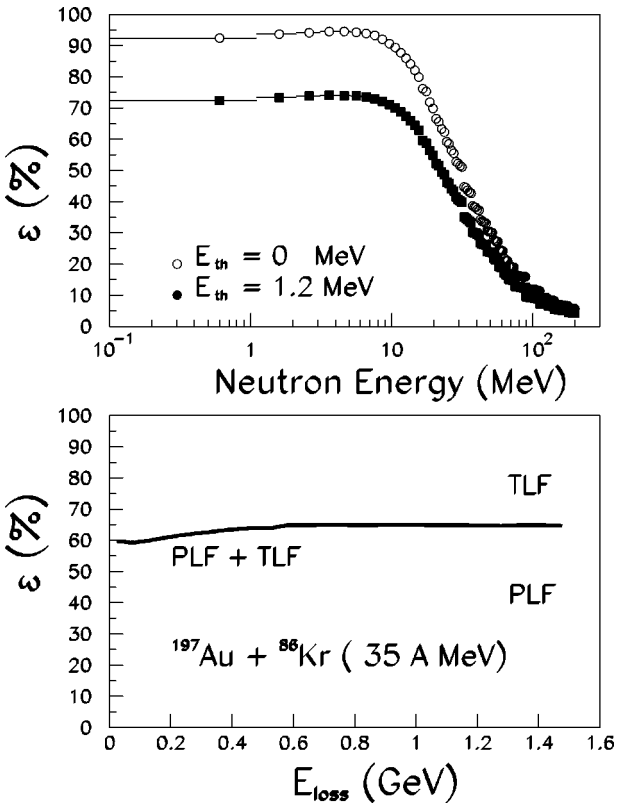

FIG. 4. Upper panel: dependence of the SuperBall detection efficiency on the neutron energy. Lower panel: dependence of the efficiency on the energy loss for the ^{197}Au+ ^{86}Kr reaction at $E/A = 35$ MeV.

and TLFs. According to the above calculations, the average (neutron capture) efficiency for the system studied in this work is $\varepsilon \sim 67\%$, with only a weak dependence on the TKEL. The observed minimum in the detection efficiency at low energy losses is attributed to the threshold for neutron emission from the excited TLFs.

Light charged products (LCPs) and IMF charged products were measured with the Washington University Microball array, configured with 86 CsI(Tl) detectors with thicknesses ranging from 4 to 10 mm. The Microball covered an angular range from 14° to 171°, representing 95% of the full solid angle, and was able to resolve p, d, t, He, Li, and Be. Atomic numbers were not resolved for $Z>4$, but these fragments were counted and included in the total IMF multiplicity m_{IMF}, discussed further below. The energy calibration of the Microball was performed by comparing the theoretical maximum energy deposits by the light charged particles in a CsI(Tl) crystal of known thickness (''punch-through'' energies) to the actually observed maximum light output in these CsI(Tl) detectors.

The experiment was set up to trigger the data acquisition whenever either a Si detector or the Microball registered an event. In such a case, signals from all charged-particle detectors were digitized and the SuperBall event was processed, generating a data stream that contained information on various correlations in the multidimensional space of experimental observables.

III. EXPERIMENTAL RESULTS AND DISCUSSION

The main aim of the experiment was directed toward the understanding of the mechanism of the heavy-residue survival in energetic heavy-ion collisions. The reaching of this goal requires that the general scenario of the reaction be reasonably well understood. The latter is possible via an analysis of various correlations between the experimental observables, not necessarily directly linked to the heavy residues.

The experimental data gathered in the present experiment consist of an event-by-event record of the experimental observables for various detected reaction products. While some of the gross features displayed by these data are characteristic of equilibrium-statistical processes, there are also numerous features seen that are indicative of a dynamical behavior. The analysis of these data, described further below, aimed first at establishing the dominant reaction scenario and the degree of its resemblance to the dissipative processes occurring at lower bombarding energies. The latter processes are well understood within the stochastic nucleon exchange model (NEM) [20] when a subsequent statistical decay of the primary reaction products is assumed, a scenario that includes both dynamical and statistical components. Therefore, the NEM was used in conjunction with the equilibrium-statistical decay model GEMINI [21] to provide a reference point for evaluating the significance of various observed characteristics of reaction products. The pursuit of such a strategy was also motivated by recent experimental findings of the persistence of dissipative binary collision dynamics at intermediate bombarding energies [22,23]. According to the

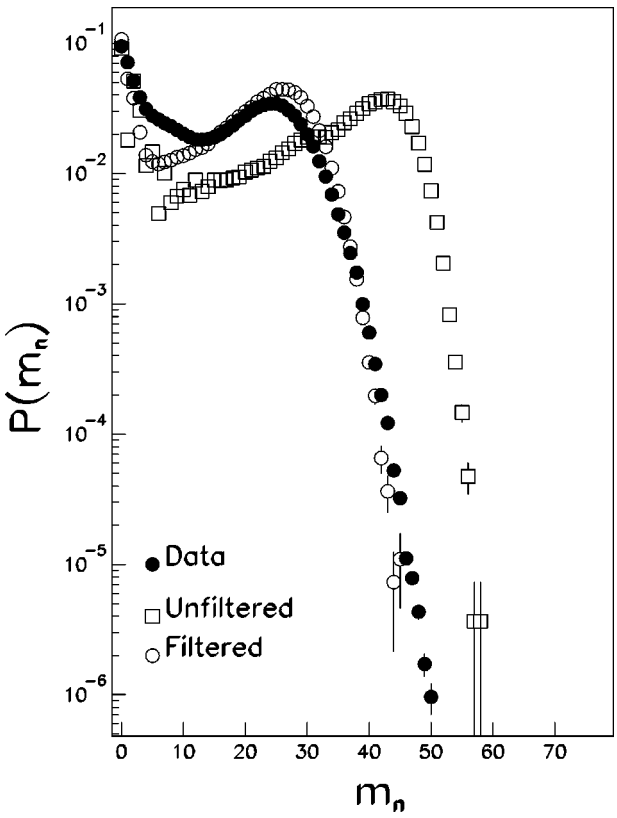

FIG. 5. Experimental neutron multiplicity (solid circles) distribution, not corrected for the detection efficiency, compared to the unfiltered (open squares) and filtered calculations (open circles) results of simulation calculations.

NEM [20], implemented here in the computer code CLAT [24], the collision dynamics and the evolution of the macroscopic system variables are governed by a combination of conservative and dissipative forces. The latter forces arise as a result of a stochastic exchange of nucleons across a ''neck'' formed transiently between the interacting massive fragments. Notably, the stochastic nucleon exchange model predicts, in agreement with experimental observations, a monotonic broadening of various distributions of the primary reaction products with increasing energy dissipation.

A. Equilibrium-statistical characteristics of the reaction product distributions

1. Particle multiplicities

The raw observed inclusive neutron multiplicity distribution is shown in Fig. 5 along with the distributions predicted by the theoretical simulation calculations. The experimental results, shown in Fig. 5 as solid symbols, are not corrected for the detection efficiency, but are corrected for the background count rate. The latter correction was achieved by unfolding the background multiplicity distribution from the directly measured distribution. The average background multiplicity depends on the beam intensity and was typically $m_n \sim 3$. The experimental neutron multiplicity distribution seen in Fig. 5 exhibits a shape that is consistent with a binary collision scenario [25] with different bins in neutron multi-

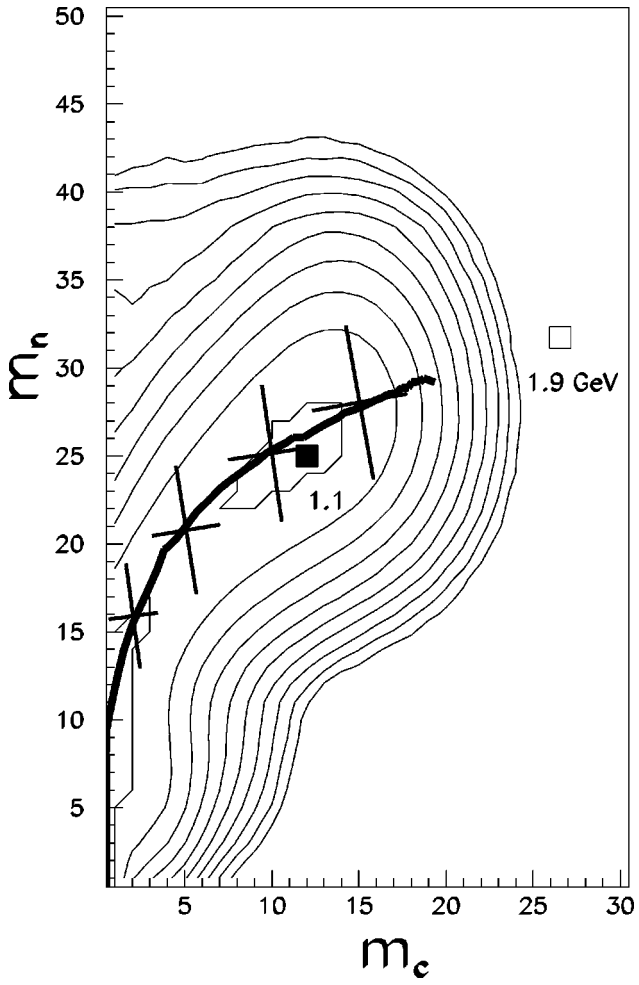

FIG. 6. Experimental joint multiplicity distribution of neutrons and charged products. The data points are the predictions of statistical model calculations for different kinetic-energy losses. See text.

plicity corresponding to different degrees in kinetic-energy damping achieved in the reaction. The most probable observed neutron multiplicity of $m_n=26$ neutrons for the central-collision bump corresponds to a true multiplicity of approximately $m_n=42$ when corrected for SuperBall efficiency. This number represents about one-fourth of all neutrons in the system.

The squares in Fig. 5 represent raw theoretical predictions by the stochastic nuclear exchange model NEM-CLAT [20,24], as combined with the equilibrium-statistical decay model GEMINI [21]. These raw simulated neutron multiplicities are not corrected for the neutron detection efficiency of the SuperBall and, hence, are expected to be systematically higher than the observed ones. However, when corrected for the neutron detection efficiency (as described in Sec. II), the model predictions (circles) agree well with the observed distribution.

While the neutron multiplicity alone provides a good measure of the total excitation energy in the system, it appears that an even better measure of this energy is provided by the joint distribution of neutron and charged-particle multiplicities. Such a joint two-dimensional multiplicity distribution for the present reaction is shown in Fig. 6 in the form of a logarithmic contour plot. The characteristic shape of the correlation ridge seen in this figure illustrates the outcome of the competition between neutron and charged-particle emission as a function of excitation energy. For peripheral collisions, associated with low to moderate excitation energies of the primary reaction products, charged-particle emission is hampered by the Coulomb barrier and, consequently, in these collisions mostly neutrons are emitted. This decay pattern is represented in Fig. 6 by the segment of the correlation ridge beginning at the origin of the plot and running parallel to the m_n axis up to $m_n \approx 15$. Charged-particle emission becomes competitive with respect to neutron emission only at higher excitation energies generated in more dissipative collisions, a behavior that is expected on the grounds of various statistical decay models. The solid line in Fig. 6 illustrates the predictions by the stochastic nucleon exchange model NEM [20,24] in conjunction with the statistical decay model GEMINI [21] as corrected for the detection efficiency. These predictions are seen to agree quite well with experimental observations.

From a quantitative comparison of the experimental data and the theoretical predictions one infers that the central-collision bump in the joint multiplicity distribution, marked in Fig. 6 by the solid square, is characterized by an excitation energy of 1.1 GeV. This energy falls well short of the 1.8–1.9 GeV energy available for the given bombarding energy to both the binary system above the barrier and to the mononuclear compound system. This limiting case of a hypothetical full damping of the kinetic energy is illustrated in Fig. 6 by the open square. Figure 6 demonstrates that in the ^{86}Kr $+$ ^{197}Au reaction at $E_{lab}/A=35$ MeV, full damping of the kinetic energy into intrinsic thermal energy is achieved only in a very small fraction of events. From an extrapolation of the joint multiplicity distribution, the possible contribution of fully damped events to the total cross section is estimated to be only $<0.1\%$.

The crossing bars in Fig. 6 illustrate the values of the covariance tensors of the joint distribution of neutron and charged-particle multiplicities, as predicted by the model calculations. Results of such calculations are shown for four different values of the assumed total kinetic-energy loss. The orientation and the length of these ''fluctuation'' bars were calculated using the method described in Ref. [26]. They represent the orientation of the major and minor axes of the covariance tensor and full width at half maximum (FWHM) of the joint multiplicity distribution in the direction of these axes, respectively. The length of these bars, i.e., the predicted fluctuations in the neutron and charged-particle multiplicities, is seen to agree with the experimental width of the correlation ridge with a 15% accuracy.

2. Charged-particle emission patterns

Further evidence for the dominantly statistical character of the light-particle production is provided by the emission patterns of the charged particles. Such patterns are best illustrated by two-dimensional Galilei-invariant yields plotted versus velocity components parallel and transversal to the source velocity. For a statistical emission from a moving

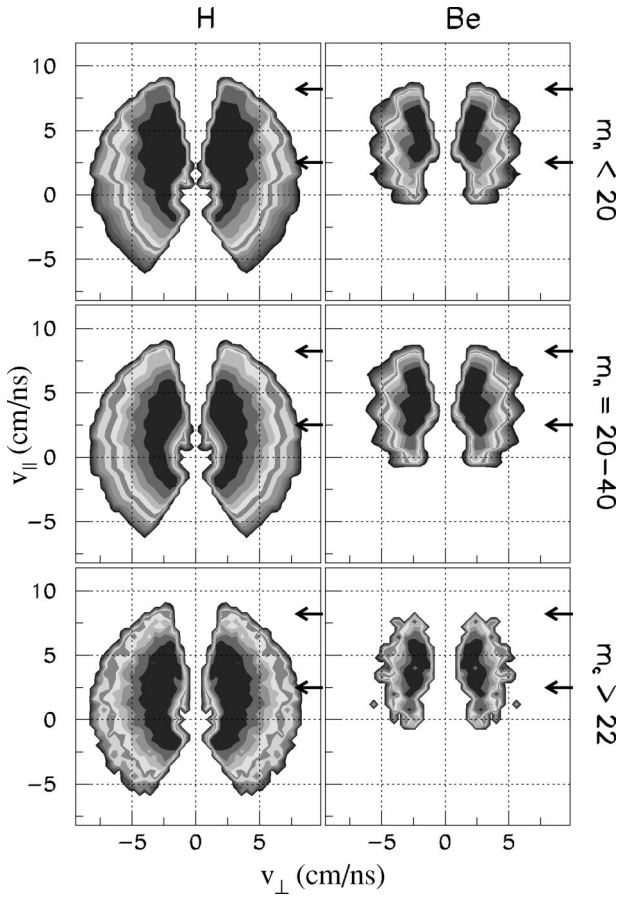

FIG. 7. Observed Galilei-invariant velocity distributions for H and Be ejectiles for three gates on the energy dissipation as selected by the neutron and charged-particle multiplicities (see text). The arrows indicate the center-of-mass and beam velocities.

excited source, the Galilei-invariant particle yield is expected to be distributed along a circular ''Coulomb ridge'' centered about the source velocity. Hence, the Galilei-invariant velocity plots of the particle yield provide a simple means of establishing the number of primary emitters and the average source velocities. Additionally, the radius of a Coulomb ridge provides information on the atomic number and the excitation energy of the associated source.

Figure 7 presents logarithmic contour plots of the observed Galilei-invariant velocity distributions for hydrogen and berylium particles emitted in three different classes of events. The upper two rows of panels were obtained by selecting the events according to the associated neutron multiplicity, while the bottom row was obtained by imposing conditions, both on neutron and charged-particle multiplicities. According to the theoretical simulation calculations, the condition $m_n > 40$ and $m_c > 22$ in the bottom row of panels selects an impact parameter window of $b/b_{max} < 0.1$.

The arrows in Fig. 7 indicate the velocities of the beam (8.2 cm/ns) and of the center of mass (2.5 cm/ns). For the light-charged particles, represented here by hydrogen ions, characteristic Coulomb ridges centered about velocities well below the velocity of the center of mass can be discerned for all three classes of events. Such emission patterns are consistent with sequential emission of particles from a slow-moving source, such as a TLF. A second Coulomb ridge is expected to be populated by the particles emitted from the PLF source. Here, it is only partially discernible due to the insufficient angular coverage of the detector setup at forward angles. The observed emission pattern is clearly inconsistent with emission from a single source, such as a hypothetical composite system moving with the velocity of the center of mass. It is worth noting that while a bimodal character of the velocity distributions is expected for low neutron and LCP multiplicities associated with peripheral collisions, such character is seen to persist also for the most dissipative, i.e., ''most central'' collisions, as selected by the prescription $m_n > 40$ and $m_c > 22$ in the bottom row of panels.

In contrast to the case of light-charged particles, the Galilei-invariant velocity distributions for IMFs, represented here by Be fragments in the right column of panels in Fig. 7, feature an intense component, characterized by a velocity intermediate between the velocity of the beam, on the one hand, and the velocity of the center of mass, on the other hand. While a circular pattern associated with emission from the TLF is present also in this case, the dominant part of the Be emission pattern is consistent with emission from a hypothetical neck zone [11–14]. The strong overall similarities to the trends observed for IMF distributions in the Bi+Xe system [11–13] already suggest that also in the present reaction, IMF production is dominated by a dynamical process involving the interface region between the two hot interacting projectilelike and targetlike fragments.

To further support the above interpretation of the observed Galilei-invariant velocity distributions, the latter were compared to the velocity distributions predicted by the combined model predictions by the CLAT [24] and GEMINI [21] codes, calculations assuming statistical emission of particles and fragments from moving PLFs and TLFs. Such model distributions, subjected to the same selection criteria as those applied to the actual data and subjected to a ''filter'' simulating the relevant features of the detector setup, are shown in Fig. 8. A comparison of this figure to Fig. 7 reveals that only for LCPs, but not for IMFs, are the observed patterns well reproduced by the simulation calculations. This observation agrees with the earlier conclusion of different mechanisms dominating in light-charged particle production, on the one hand, and IMF production, on the other hand.

B. Dynamical characteristics of the reaction product yields

In the previous subsection, Sec. III A, it was shown that the yields of IMFs observed in the present study cannot be reconciled with a purely statistical production scenario, pointing to the dominantly dynamical character of the IMF production. The dynamical characteristics of the product yields are discussed in more detail in the following subsections.

1. Characteristics of IMF production

The previous discussion of the charged-product emission patterns suggested that the IMF yield cannot be accounted for solely by a pure statistical emission from PLF and TLF.

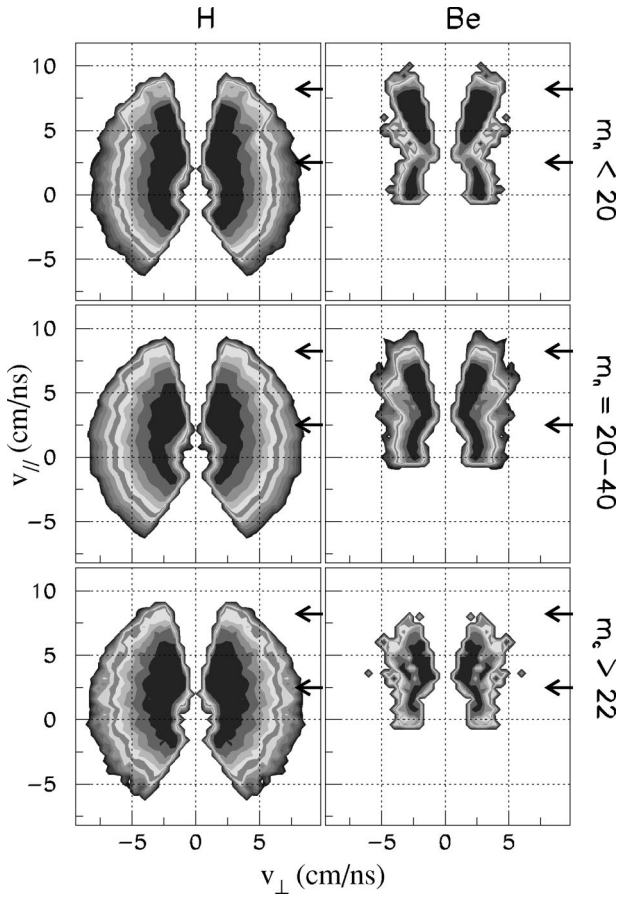

FIG. 8. Simulated Galilei-invariant velocity distributions for H and Be ejectiles for three gates on the energy dissipation as selected by the associated neutron and charged-particle multiplicities (see text). The arrows indicate the center-of-mass and beam velocities.

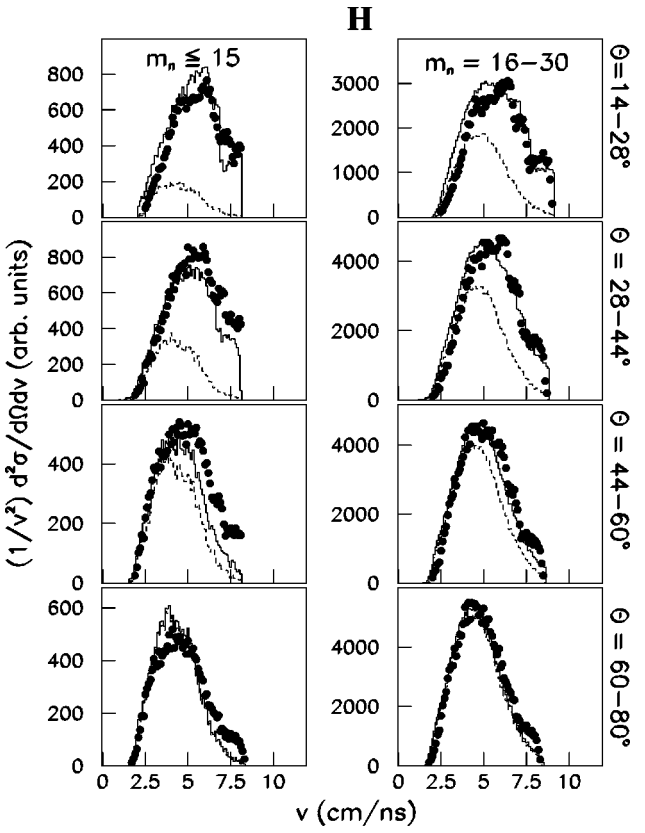

FIG. 9. Experimental (dots) and simulated (histograms) velocity distributions for hydrogen ions for different neutron multiplicities and emission angles. The dashed histogram represent yield contributed by the TLF decay.

To further assess the contribution of a nonevaporative source to the IMF yield a quantitative comparison of the simulated velocity distributions data to the measured distributions is presented in Figs. 9 and 10. Here, the experimental (solid symbols) velocity distributions for hydrogen and berylium ions, H and Be, respectively, are plotted, along with the calculated (histograms) distributions. These velocity distributions were obtained for the indicated emission angles of the charged particles and two different bins in the associated neutron multiplicity. The left column corresponds to partially damped peripheral collisions with $m_n < 15$, while more dissipative collisions, with $m_n = 16-30$, are illustrated by the column on the right-hand side. A relative normalization of the theoretical velocity spectra to the data was performed by normalizing the spectra obtained at the most backward angles, where the contribution from the TLF is expected to dominate. The calculated velocity spectra evolve in a smooth manner with increasing emission angle (top to bottom). At small emission angles, the spectrum is dominated by a contribution by the PLF source, while at backward angles it is essentially due only to the emission from the TLF source. The component associated with the emission from the TLF, as inferred from the calculations, is shown in Figs. 9 and 10 by a dashed histogram. Correspondingly, at intermediate angles the spectrum has a double-humped shape corresponding to a superposition of two components associated with the emission from PLF and TLF, respectively. For the light particles, represented in Fig. 9 by the hydrogen ions H, the calculated spectra reproduce reasonably well the observed distributions. In contrast, the measured IMF velocity distributions shown in Fig. 10 show a significant contribution at intermediate velocities, in excess of those attributed to PLFs and TLFs. This excess component is present for all impact parameters. According to the calculations, a good kinematical separation of components of IMFs from PLFs and TLFs leaves the intermediate-angle range free of IMFs. Most IMFs observed here must come from a different source. As the calculations assume that the IMFs are emitted statistically from exited PLFs and TLFs, this component is identified as the neck zone dynamical contribution.

From the above observations and observations of similar character made for other systems [22,27], one concludes that, at these intermediate energies, heavy-ion reactions are dominated by dissipative dynamics. For midperipheral to central collisions, IMFs appear to be produced at the interface or necklike zone. Subsequently, the excited PLFs and TLFs reseparate and undergo a sequential statistical decay.

2. IMF multiplicity distribution

The observed IMF multiplicity distribution is shown in Fig. 11 (solid symbols). This distribution was measured with

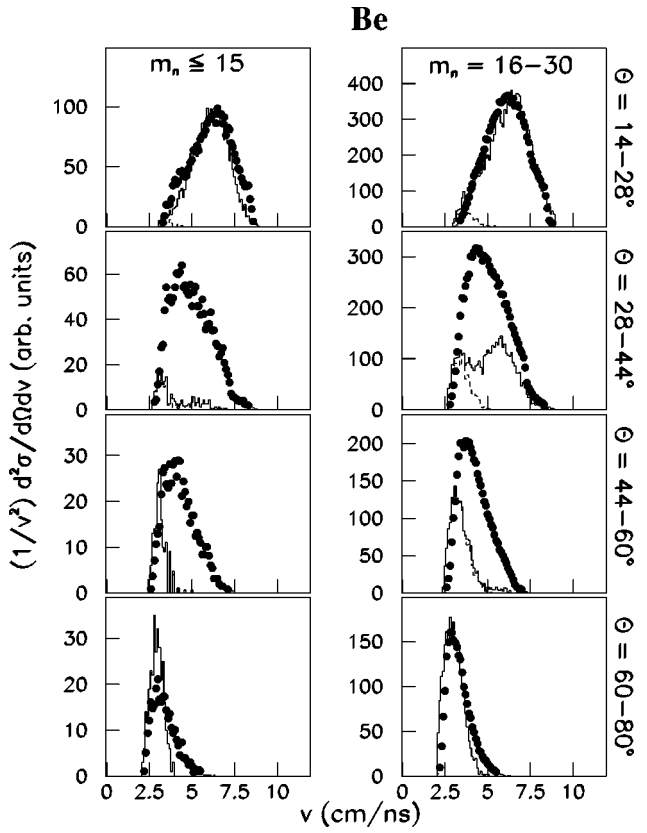

FIG. 10. Same as Fig. 9, except for Be ions.

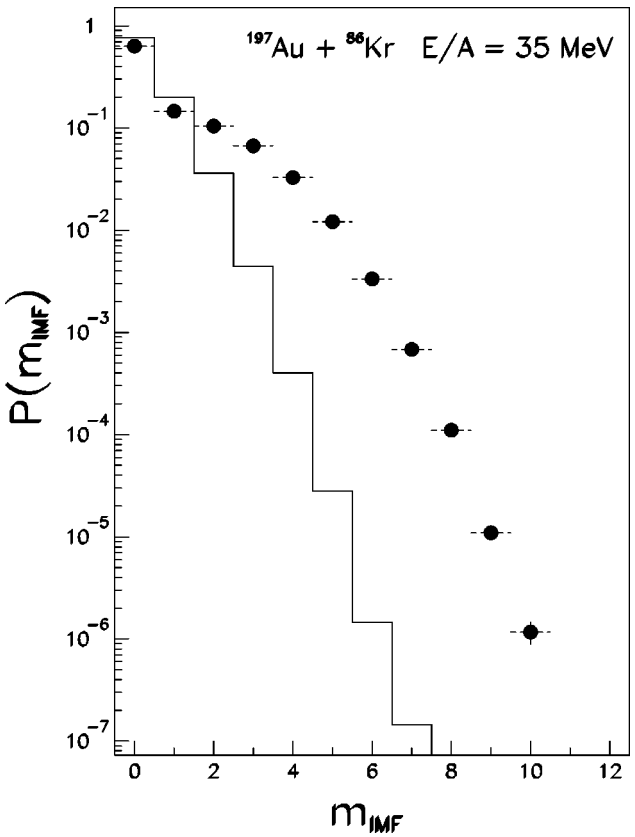

FIG. 11. Experimental (solid dots) and theoretical (histogram) IMF multiplicity distributions.

a ''minimum-bias'' trigger requiring that at least two sectors of the SuperBall register signals in coincidence. As can be evaluated from this distribution, the events with two or more IMFs constitute ~25% of the total yield measured with the ''minimum-bias'' trigger. When a different ''low-bias'' trigger is used, requiring the detection of at least one charged particle in the Microball, i.e., $m_c \geqslant 1$, the contribution of the multiple IMFs events is even larger, ~35% of all events. From these considerations, it is clear that in the energy domain of the present study, multiple IMF production constitutes an important reaction channel, accounting for a sizable fraction of the total reaction yield. For comparison, the calculated IMF multiplicity distribution is shown in Fig. 11 as a histogram. In the calculations it has been assumed that IMFs are emitted statistically from exited PLFs and TLFs. It is clear from this comparison that the observed multiplicities are significantly higher than can be explained by statistical-model calculations.

C. Characteristics of projectilelike fragments

1. Elastic scattering

In order to determine the total reaction cross section, the angular distribution of the elastic-scattering yield was analyzed. The latter information was obtained using position-sensitive detector telescopes placed at forward angles. The elastic-scattering yield was extracted from the energy spectra measured for each of the individual strips in the second constituent detectors of the telescopes. Absolute calibrations of the angles relative to the actual beam axis and the normalization of the measured yields were achieved by fitting the measured elastic angular distribution at very forward angles to the corresponding Rutherford cross sections. The procedure resulted in the elastic-scattering–to–Rutherford yield distribution shown in Fig. 12. This angular distribution is of the Fresnel type, indicating the dominance of Coulomb effects for heavy systems at this bombarding energy. From the distribution shown in Fig. 12, the grazing angle was deduced using the quarter-point method [28], $\theta_{gr}^{\mathrm{c.m.}} = (8.9 \pm 0.6)°$, $\theta_{gr}^{lab} = (6.1 \pm 0.4)°$. The corresponding maximum angular momentum and total reaction cross section were found to be $l_{max} = (972 \pm 71)\hbar$ and $\sigma_R = (5.0 \pm 0.7)$ b, respectively. These values are in good agreement with the systematics [29] established at lower bombarding energies, predicting $l_{max} = 1023\hbar$ and $\sigma_R = 5.5$ b for the present system.

2. Energy and charge distributions

Figure 13 depicts a two-dimensional contour diagram of the yield of charged reaction products observed within the angular range covered by the forward telescopes, plotted versus atomic number ($Z_{PLF} > 5$) and energy of the product. As seen in Fig. 13, this yield is concentrated along a well-defined ridge connecting in a continuous fashion the region of elastic and quasielastic events ($Z_{PLF} \approx 36$ and $E/E_{beam} \approx 1$), with that of the IMFs near the origin of the plot. One notes that this ridge is free of major contaminations by fission fragments originating from TLF fission or from a sym-

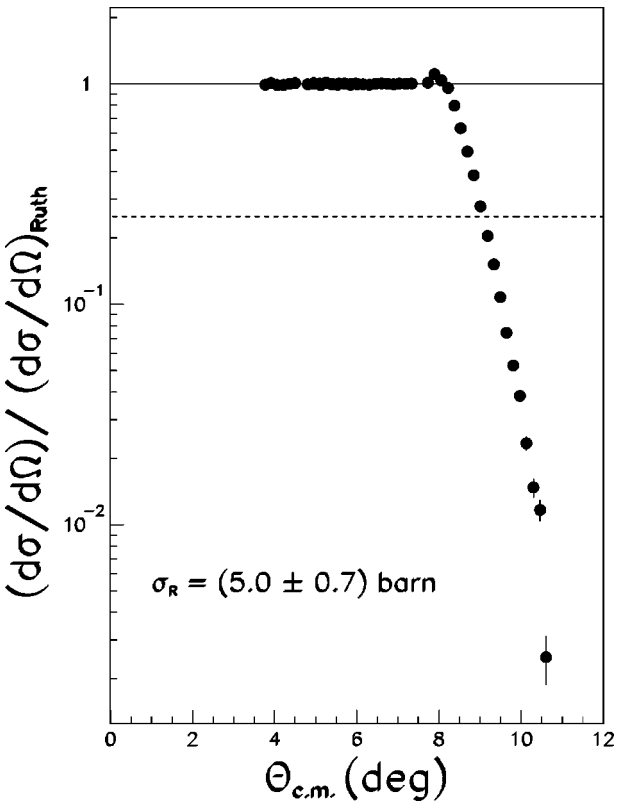

FIG. 12. Ratio of the elastic–to–Rutherford-scattering cross sections. The dashed line illustrates the quarter-point yield.

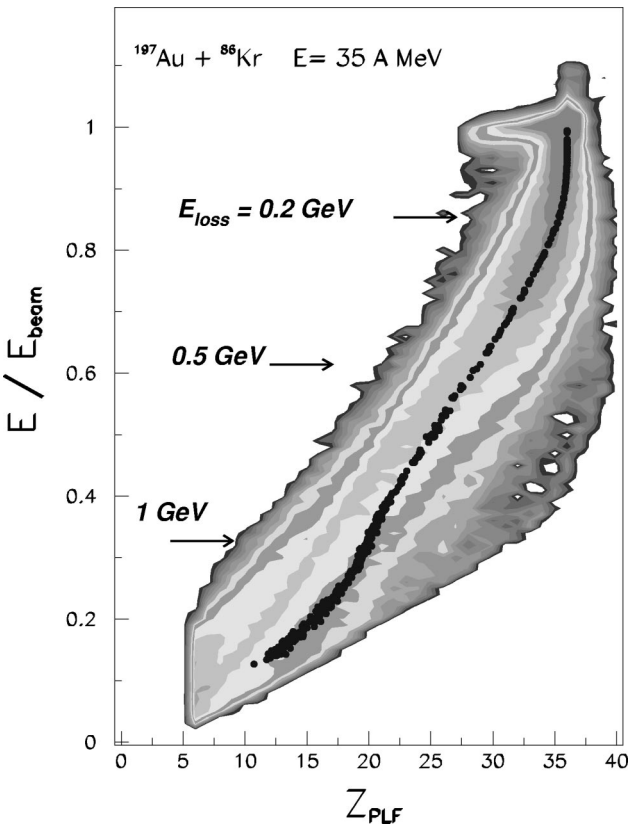

FIG. 13. Contour diagram of the yield of charged reaction products from the ^{197}Au+ ^{86}Kr reaction, observed in an angular range 1.9°–9°, plotted versus kinetic energy, normalized to beam energy, and atomic number of the product. The data points are the predictions of statistical calculations for different energy losses, as discussed in the text.

metric PLF fission. This behavior is expected, because the energy of the former is insufficient to overcome the charge identification threshold of the telescopes and there is no evidence for a bimodal yield pattern associated with PLF fission, as observed in previous studies [30] for much heavier projectile. The dots in Fig. 13 refer to the predictions by the calculations described above for an energy loss ranging from 30 MeV to 1.4 GeV. The calculations assume a dissipative binary dynamics of the collision, followed by a sequential, statistical decay of the emerging excited PLFs and TLFs. It was found in these calculations that the observed secondary yield does not depend significantly on the excitation energy division between the two reaction partners. The calculations reproduce well the observed trend for PLF atomic numbers close to that of the projectile. For higher energy losses, corresponding to an observed PLF atomic number $Z_{PLF}<20$, the PLF atomic number is overestimated by the model calculations. This discrepancy can be explained by the role of IMF production in reducing Z of the primary PLFs. An estimate for the total cross section for the PLF production can be obtained by integrating the observed yield over the energy of the products and by extrapolating it to the angular range not covered by the telescopes. Such an estimate resulted in the cross section $\sigma_{PLF}\approx(3.7\pm0.9)$ b.

3. Deflection function

The dynamics of heavy-ion collisions is best reflected in the deflection function illustrating the dependence of the emission angle on the impact parameter. With the impact parameter unavailable for a direct measurement, in the study of dissipative heavy-ion collisions at energies of a few MeV/nucleon above the interaction barrier, a somewhat different representation of the deflection function is commonly used, first suggested by Wilczyński [31]. In this representation, the total kinetic-energy loss is plotted versus deflection angle. In the Fermi-energy domain of bombarding energies, the measurement of the TKE becomes a complex process, reducing the usefulness of the original Wiczyński representation. In this domain of bombarding energies the deflection function is suitably represented by the dependence of the PLF energy or the neutron multiplicity on the PLF emission angle.

The upper-left panel of Fig. 14 shows the correlation between the measured E/Z ratio and the measured emission angle for all charged reaction products with $Z>5$. The E/Z ratio provides a quadratic velocity scale of the secondary PLF fragments. Assuming that the secondary PLFs are produced from the primary ones as a result of statistical decay, the average emission angle of a secondary reaction product is approximately equal to the average emission angle of the primary PLF and, hence, refers to the average collision dynamics.

As seen in Fig. 14, the fragment yield is distributed along a Z-shaped ridge. The upper, intense section of this ridge is due to elastic and quasielastic scattering. The second section

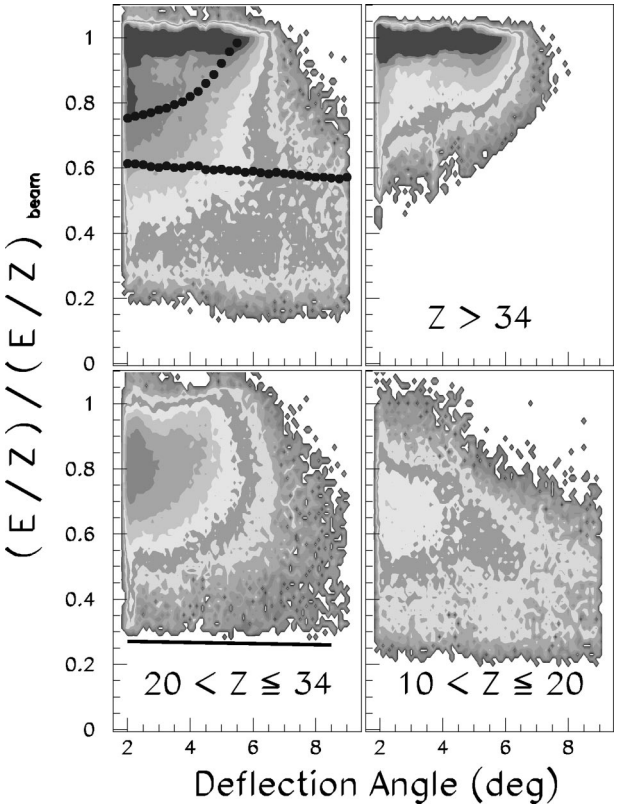

FIG. 14. Experimental deflection-function plots for different bins in the atomic number of the associated PLFs (contour plots), compared with the theoretical average trends (solid dots). See text.

of the ridge is due to the partially damped collisions and is seen to extend from the grazing region toward lower velocities and forward angles. A less distinct, third section of the yield ridge is discernible in Fig. 14, extending from forward angles toward lower velocities at angles beyond the grazing angle ($\theta_{gr}=6.1°$). The observed correlation is reminiscent of the Wilczyński plots illustrating the deflection function for dissipative heavy-ion collisions at energies of a few MeV/nucleon above the interaction barrier. Similar results were obtained recently at intermediate bombarding energies [23,32]. The solid dots in Fig. 14 represent the results of theoretical model calculations using the codes CLAT [24] and GEMINI [21]. These calculations are seen to predict an increasing orbiting of the dinuclear system with increasing energy dissipation. According to these calculations, the third segment of the yield ridge is associated with negative deflection angles.

The remaining panels of Fig. 14 represent a decomposition of the yield seen in the upper left panel according to the measured atomic number of the PLF remnant, as indicated in each panel. As the atomic number of the PLF remnant decreases, the angular distribution of the fragments is seen to broaden with a simultaneous slowing down of the PLFs. These trends are consistent with a dissipative orbiting process, as observed [23] in a study of the ^{209}Bi+ ^{136}Xe reaction at $E/A=28$ MeV. In both cases, an increased deflection of the PLFs relative to Coulomb trajectories is accompanied by increased energy dissipation. However, while the calculations reproduce qualitatively the average experimental features of the Wilczyński plot, the theoretical dissipation is stronger than observed experimentally. This discrepancy is particularly clear for the partially damped middle segment of the yield ridge in Fig. 14. The strong theoretical friction forces lead eventually to a "sticking" of the interacting fragments and a large theoretical cross section for fusion ($\sigma_{fus}\sim 1.8$ b). Experimentally, no evidence was found for such fusion events.

4. Excitation-energy division

One of the most characteristic features of damped collisions is the conversion of a significant part of the initial collective kinetic energy into intrinsic excitation energy of the reaction partners in an irreversible dissipative process. In the energy balance for the reaction, the dissipated kinetic energy makes up for the sum of excitation energies of the primary fragments. The way in which this excitation energy is divided between the two primary fragments reflects the properties of the heat generation and relaxation mechanisms [33] and is, hence, a useful experimental observable.

In the present study, the excitation-energy division was evaluated based on a comparison of the proton emission patterns for different total excitation energies to those predicted by the NEM [20,24] and GEMINI [21] model calculations described in the previous sections. To that goal, the emission pattern was described by just one parameter η reflecting the forward-backward asymmetry of the proton yield:

$$\eta=\frac{\Sigma m_{back}-\Sigma m_{\rm for}}{\Sigma m_{back}+\Sigma m_{\rm for}}, \tag{1}$$

where m_{for} and m_{back} represent the proton multiplicities measured in the angular ranges of 14°–28° and 128°–147°, respectively. These two angular ranges are covered by the most forward and most backward rings of the Microball array, respectively.

The results of the model calculations for different total excitation-energies and different assumed excitation energy divisions are shown in Fig. 15. The upper left panel is for inclusive results, while the remaining ones are for the individual bins in neutron multiplicity, used here as a measure of the total thermal excitation energy of the system. The horizontal solid lines shown in each panel illustrate the experimental asymmetry η of the proton emission patterns. Utilizing the fact that the model predictions show a distinct dependence on the excitation energy division, the latter quantity can be then determined from the requirement that the model prediction agree with the experimental observations, i.e., from the intersection point of the theoretical line and the horizontal line representing the experimental result.

The resulting dependence of the excitation-energy division on the total excitation energy is illustrated in Fig. 16, where the ratio of PLF and TLF excitation energies *per nucleon* is shown as a function of the total excitation energy. In this figure, a smooth transition is seen to occur with increasing total excitation energy from a near equipartition of the total excitation energy to the limit of thermal equilibrium

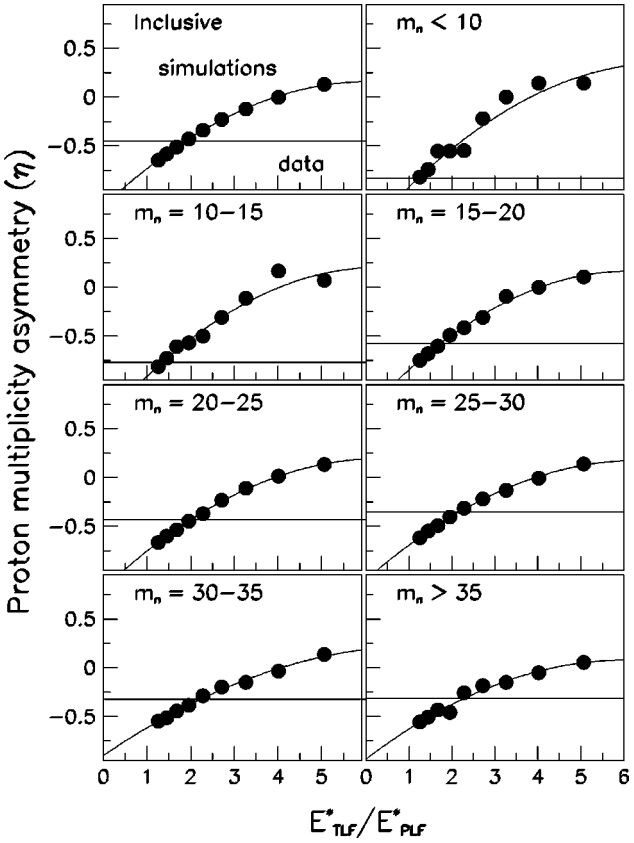

FIG. 15. The forward-backward asymmetry in the proton yield as predicted for the theoretical model calculations (solid dots and lines) for various degrees of kinetic-energy dissipation and various excitation-energy divisions. The horizontal lines indicate the respective experimental values.

division. In the latter mode of energy division, the individual excitation energies of PLFs and TLFs are in a direct proportion to their respective mass numbers. Figure 16 suggests also that complete thermal equilibrium may not have been

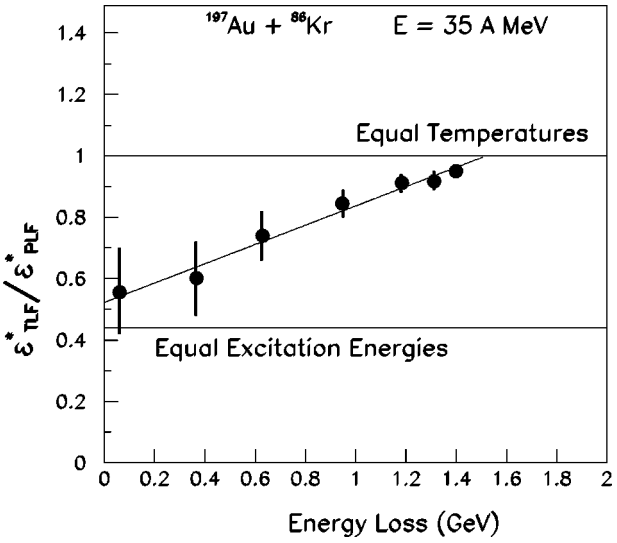

FIG. 16. Excitation-energy division as a function of the total excitation energy.

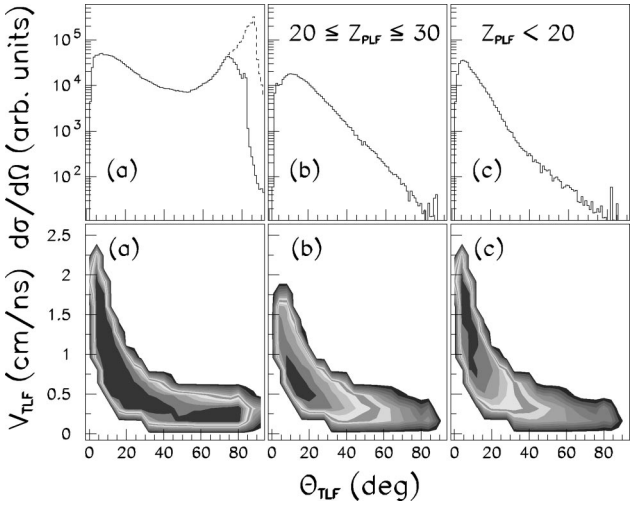

FIG. 17. Angular distributions (top) and velocity versus angle correlations for TLFs, as deduced based on the PLF data, for various bins in Z_{PLF} as indicated in the panels. The leftmost column is for inclusive data.

reached in this reaction for the classes of events selected according to the associated neutron multiplicity.

D. Heavy-residue production

Heavy residues are defined in the present study as massive remnants of the primary targetlike fragments. These remnants result from either particle evaporation or fission. The former are expected to have low velocities due only to the recoil experienced by TLFs in the course of the dissipative collision.

1. Properties of targetlike fragments

Figure 17 illustrates selected qualitative and quantitative characteristics of the targetlike fragments as deduced from the experimental data for the measured projectilelike fragments. The TLF characteristics were deduced under the assumption that the collision is governed by binary dissipative dynamics and that the primary products of the collision, the PLFs and TLFs decay into the observed secondary fragments via sequential statistical evaporation of particles. Accordingly, it was assumed that the velocity vectors of the primary and secondary fragments coincide. The upper panels of Fig. 17 show the reconstructed angular distributions of TLFs, while the lower panel show the contour diagrams of the TLF yield plotted versus the recoil angle and recoil velocity. The panels are organized in columns characterized by different conditions on the atomic number Z_{PLF} of the detected PLF. The dashed curve in the upper leftmost panel *a* represents the total TLF angular distribution including the elastic and quasielastic events; i.e., this line represents most of the yield at $\theta_{lab} \sim 90°$. The exclusion of the elastic and quasielastic events leads to the distribution represented by the histogram drawn as a solid line and contour diagram (a). A selection of more dissipative collisions, characterized by lower atomic numbers of the PLF, as indicated in panels (b) and (c), leads to more forward-peaked TLF angular distributions and

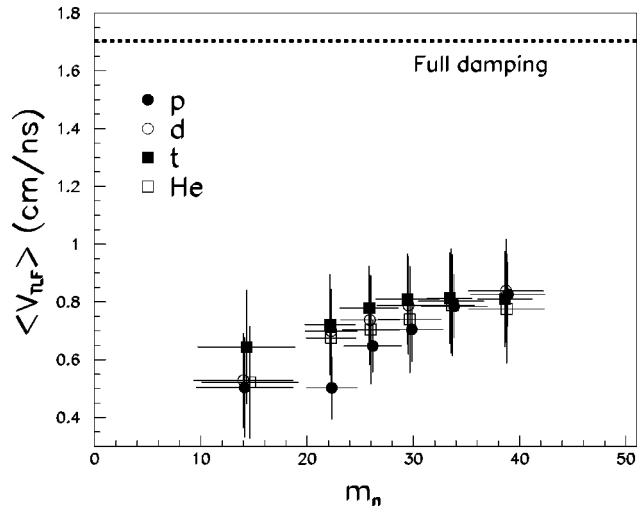

FIG. 18. The correlation between the velocity of TLFs and the associated neutron multiplicity, as deduced from Galilei-invariant velocity plots of hydrogen and helium ions.

higher TLF recoil velocities as the transferred linear momentum increases. Note that the rapid drop of the TLF angular distribution around $\theta_{TLF} \sim 0°$ is an experimental artifact due to the absence of PLF data at backward angles.

By comparing the above deduced TLF characteristics to the experimental observations from the study of the ^{197}Au $+ \, ^{129}$Xe reaction [34] at $E/A = 21$–44 MeV/nucleon, one concludes that these TLF residues are associated with quasielastic and damped-reaction processes. For those TLFs whose mass number is close to that of the target, the degree of the energy damping is low and, accordingly, the angular distribution is peaked sidewise. In addition, these fragments have low (recoil) velocities. As the degree of the energy dissipation increases, the observed secondary masses of TLFs and PLFs decrease and the associated linear momentum transfer results in an increase of the recoil velocity of TLFs and in their more forward-peaked angular distributions.

The TLF recoil velocities were also deduced independently from the Galilei-invariant velocity plots of the emitted light-charged particles. At backward angles, the observed LCPs are mostly associated with the emission from TLFs and, therefore, their velocity distribution reflects the kinematic boost due to the movement of TLFs. These velocity distributions measured at backward angles were analyzed [16] for different bins in the degrees of kinetic-energy dissipation achieved. As a measure of the latter quantity, neutron multiplicity was used.

The evolution of the average TLF recoil velocity with increasing energy dissipation is shown in Fig. 18, as deduced independently from the velocity distributions of hydrogen and helium ions. In this figure, the TLF recoil velocity is seen to increase with increasing kinetic-energy dissipation, but far from the ''full-damping'' [35] limit of 1.7 cm/ns for the present system. This observation proves that even for the most dissipative collisions selected according to measured neutron multiplicities, the damping of the kinetic energy is incomplete. Similar conclusions were reached earlier in the

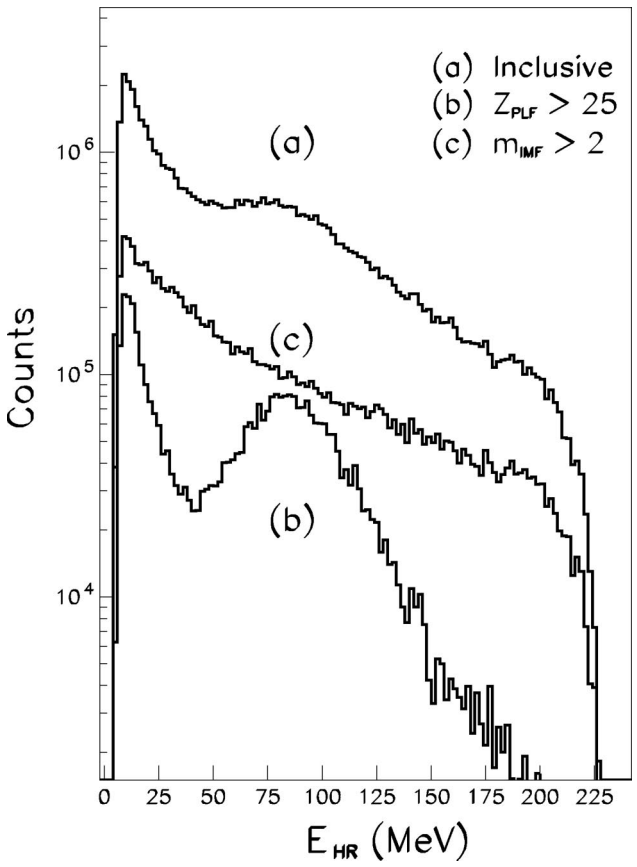

FIG. 19. Inclusive (a) and exclusive (b) and (c) energy spectra of heavy residues. The exclusive spectra are for moderately (b) and highly (c) dissipative collisions.

studies of the ^{197}Au$+ \, ^{208}$Pb reactions at $E/A = 29$ MeV [30], the ^{209}Bi$+ \, ^{136}$Xe reactions at $E/A = 28$ MeV [11], and the ^{112,124}Sn$+ \, ^{124,136}$Xe reactions at $E/A = 55$ MeV [3].

2. Identification of the slow, heavy residues

A more complete identification of heavy residues and, in particular, their distinction from the PLF residues and intermediate-mass fragments was achieved via the joint measurement of their time of flight and energy. This is seen in Fig. 3 where the TLF residues are represented by the upper branch in the upper panel. This upper branch represents both fission fragments and the evaporation residues as is seen in the lower panel of Fig. 3, where a coincidence was required with a massive PLF ($Z > 25$).

Inclusive and exclusive angle-integrated HR energy spectra (not corrected for the pulse height defect) are shown in Fig. 19. These spectra were measured under the following conditions: (a) in inclusive mode, (b) in coincidence with a massive PLF ($Z_{PLF} > 25$), and (c) in coincidence with at least three IMFs detected in the Microball. The significance of the latter criterion is discussed further below. The energy spectra (a) and (b) are similar to each other and exhibit two components: a Gaussian-like distribution, centered about ~ 90 MeV, and a superimposed broad exponential-like distribution. The former component exhibits the characteristics expected for fission fragments (HR-FF), as ascertained by

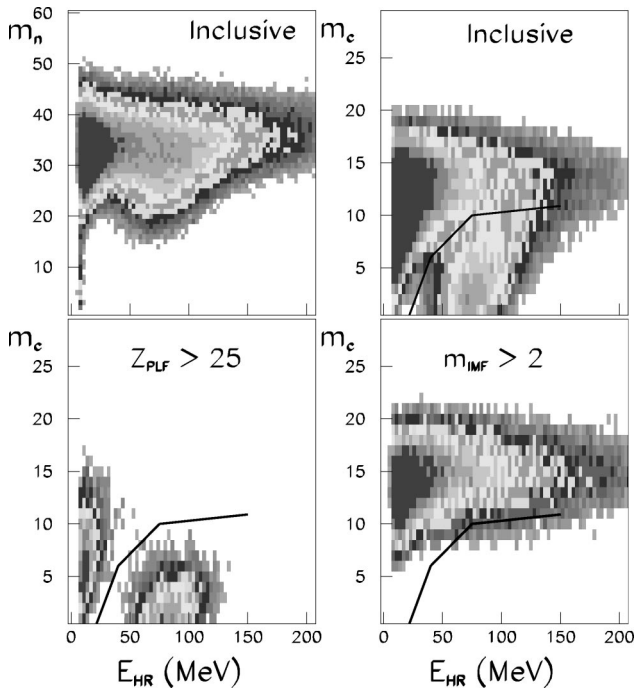

FIG. 20. Contour plot of the heavy-residue yield, plotted versus the heavy-residue energy and particle multiplicity. The panels are for different conditions on the associated reaction observables, as indicated. Solid lines indicate the suggested separation line between fission fragments and evaporation residues.

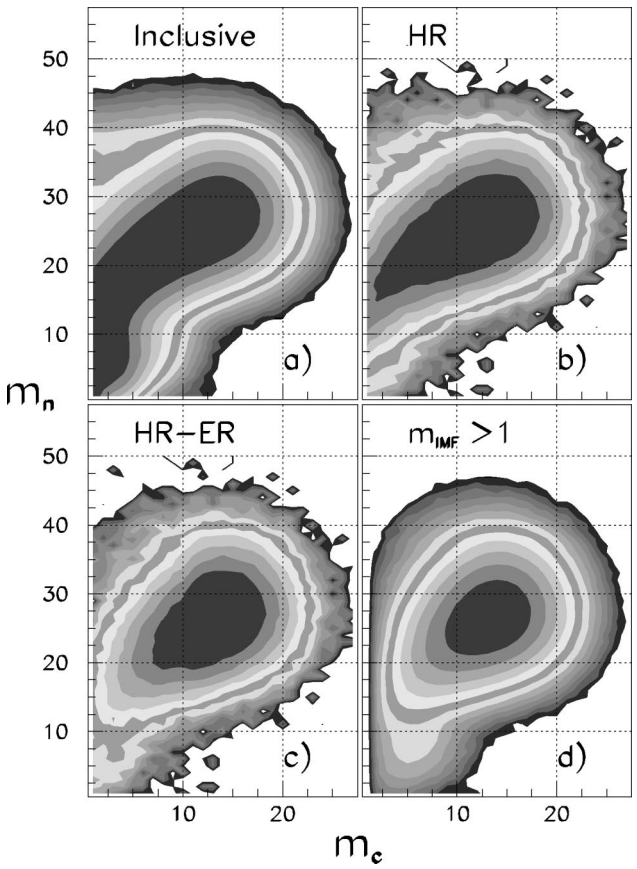

FIG. 21. Contour diagrams of joint distribution of neutron and charged product multiplicities for all events (a) and classes of events associated with heavy residue production (b), TLF evaporation residue production (c), and IMF multiplicities $m>1$ (d).

the calibration performed with the fission fragments from a ^{252}Cf source. The fragments associated with the monotonously decreasing HR component are identified as TLF evaporation residues and are denoted as HR-ER in the following.

In order to obtain a further characterization of the two HR components, in Fig. 20 the HR yield is plotted versus the HR energy and the multiplicities of neutrons or charged particles. In this figure, the same conditions were used conditions as in Fig. 19. As seen in the upper left panel of Fig. 20, the heavy-residue production is associated with high neutron multiplicities corresponding to the high-multiplicity ''bump'' in the neutron multiplicity distribution of Fig. 5. This proves that HRs are mostly produced in highly dissipative collisions. On the other hand, the correlation of HR energy with the associated charged particle multiplicity, m_c, allows one to separate the two components observed in the projected spectra (a) and (b) of Fig. 19. The HR-ER component is seen to be associated with larger values of m_c than the HR-FF one. Similar observations were made in earlier works [36] devoted to HR. Of special interest is the fact that the E_{HR} versus m_c correlation plots provide for a good separation of the two components when the coincidence with massive PLFs with $Z_{PLF}>25$ is required. This is seen in lower left panel of Fig. 20.

3. Correlations between heavy residues, projectilelike fragments, and light-particle multiplicities

Figure 21 offers a characterization of various classes of events according to the total excitation energy measured by the joint distribution of neutron and LCP multiplicities. Panel (a) shows the inclusive joint multiplicity distribution that was introduced earlier in Sec. III A. The characteristic correlation ridge in this plot reflects the evolution of the system characteristics with increasing kinetic-energy loss and presumably decreasing impact parameter. Panel (b) shows the joint neutron versus LCP multiplicity distribution for a class of events in which a HR was detected and identified in the multistrip detector setup. As pointed out above, the events in this class are associated mostly with highly dissipative collisions. The apparent absence of events with low total excitation energies, characterized by low LCP and neutrons multiplicities, is due to the fact that TLFs from peripheral collisions, mainly quasielastic, are emitted at large angles not covered by the detector setup and would be very difficult to measure anyhow, because of their very low energy. Panel (c) in Fig. 21 presents the joint neutron versus LCP multiplicity distributions measured in coincidence with evaporation residues, HR-ER. The events in this class belong mostly to the most dissipative ones $[m_c,\ m_n \approx (12,25)]$ when compared to the inclusive distribution. Consequently, the HR-FF yield is due mostly to peripheral and midperipheral collisions, while the HR-ER yield arises from midperipheral to central collisions, for which also IMFs are produced. The latter conclusion is further supported by the plot shown in panel (d),

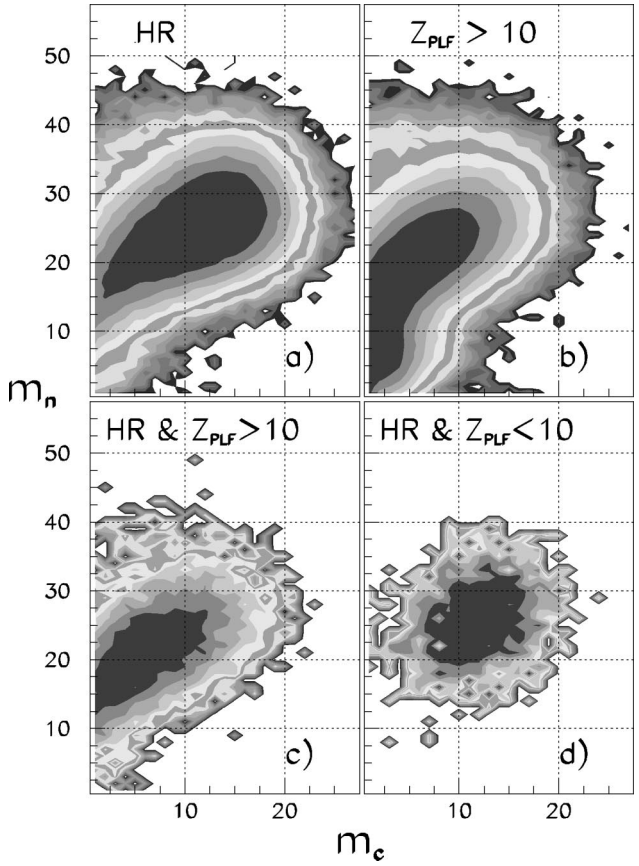

FIG. 22. Same as Fig. 21, except for different conditions on heavy residues and Z_{PLF}, as indicated in the panels.

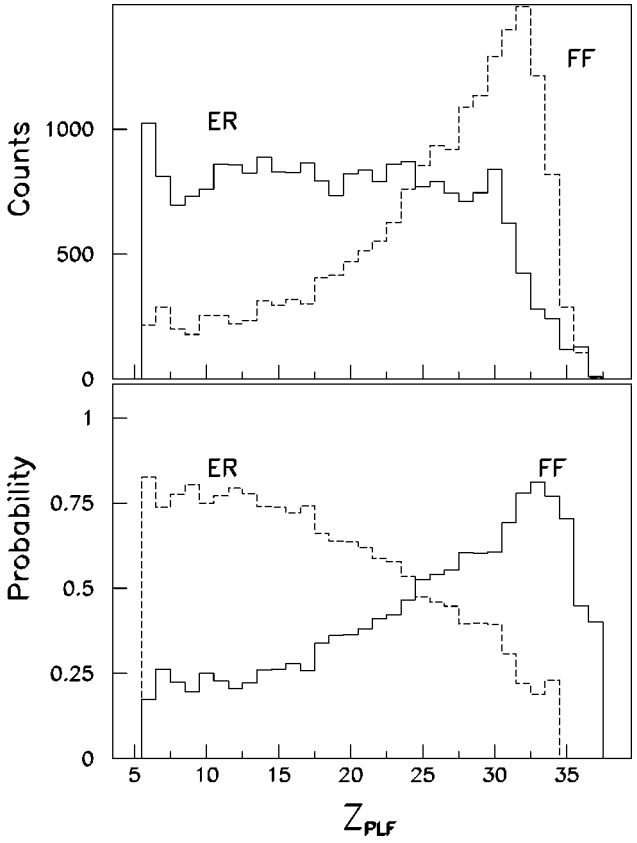

FIG. 23. Atomic-number distributions for PLFs observed in coincidence with TLF fission fragments (dashed lines) and TLF evaporation residues (solid lines) (top panel) and the same distributions divided by the inclusive Z_{PLF} distribution (bottom panel).

obtained for the events where at least two IMFs are detected in the Microball, but without requiring a coincidence with a PLF or a HR. Clearly a coincidence requirement of two IMFs also selects dissipative events, similarly to the HR-ER coincidence requirement, discussed further above.

Figure 22 illustrates the correlations between HR and PLFs. Panel (a) shows the joint neutron versus LCP multiplicity distribution for a class of events in which a HR was detected. Panel (b) shows the joint neutron versus LCP multiplicity distribution for a class of events in which a PLF with an atomic number $Z_{PLF} \geqslant 10$ is detected in a PLF telescope. The latter condition selects mostly peripheral and midperipheral collisions. Requiring the coincidence of a HR and a PLF with $Z_{PLF} \geqslant 10$ leads to the joint m_n versus m_c multiplicity distribution shown in panel (c). The observed shift toward lower multiplicities in the distribution (c), with respect to that shown in panel (a), allows one to conclude that very few (secondary) PLFs with $Z_{PLF} \geqslant 10$ emerge from the most dissipative collisions. In contrast, by selecting the most dissipative collisions through the requirement of the coincidence of a heavy-residue and a fragment with $5 < Z < 11$ in the PLF telescopes (i.e., at forward angles), one obtains the exclusive distribution shown in panel (d).

One concludes from the above data that for the most dissipative collisions, either the size of the primary PLF is significantly reduced and/or the PLF breaks up into several IMFs.

Further quantitative analysis of the heavy residue data is presented in Fig. 23. The upper panel of Fig. 23 shows the Z distribution of PLFs measured in coincidence with evaporation residues and fission fragments. While the TLF evaporation residues (HR-ER) are associated with a broad range of PLF atomic numbers, the TLF fission fragments (HR-FF) are associated mostly with the production of massive (secondary) PLFs with atomic numbers close to that of the projectile. As these distributions are weighted with the actual impact parameter distribution, a corresponding production probability distribution may be obtained by dividing the above distributions by the inclusive PLF atomic number distribution. The results of such an ''unfolding'' are illustrated in the lower panel of Fig. 23. As seen in this panel, there is a large shift in the average Z of the PLF toward higher Z values for the events associated with TLF fission. This demonstrates that the TLF evaporation residues are produced in the most dissipative collisions, while for the less dissipative collisions the primary TLF tends to decay by fission.

4. IMF production and the survival of HRs

Further evidence for a production scenario in which the heavy residues are TLF remnants is obtained from Galilei-invariant velocity distributions for light-charged particles. Such distributions are shown in Fig. 24 for He and Be ions for three bins in the associated neutron multiplicity and for

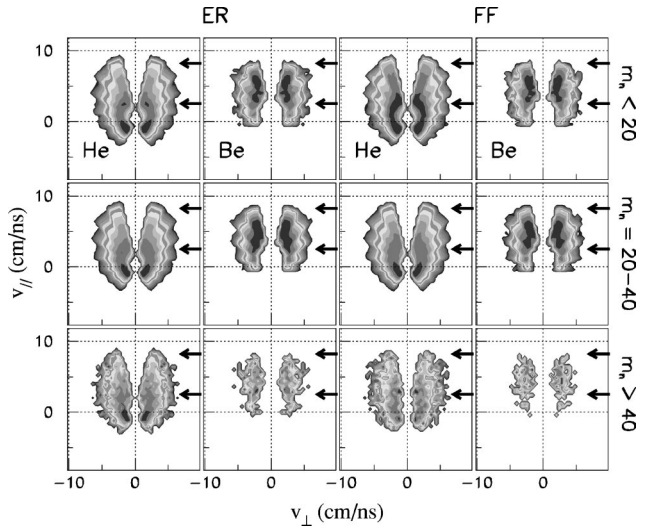

FIG. 24. Galilei-invariant velocity plots for helium and berylium ions detected in coincidence with TLF fission fragments (two top rows) and TLF evaporation residues (two bottom rows), for different degrees of energy dissipation as measured by the associated neutron multiplicity (different columns).

both components observed in the energy distributions of Fig. 19(a). As seen in Fig. 24, for the entire range of energy dissipation, the light-charged-particle velocity distributions exhibit quite well-defined Coulomb ridges, pointing to a sequential emission from slow-moving sources. Thus, the previous identification of HRs measured in coincidence with massive PLFs as TLF remnants is seen to be valid for the entire set of HR events measured in this experiment.

It is worth noting that IMF invariant velocity distributions measured in coincidence with HRs, shown in Fig. 24, exhibit similar patterns in comparison to the inclusive velocity distributions (see Fig. 7). This similarity is indicative of IMFs being produced in the interface zone between (primary) PLFs and TLFs, with HRs being TLF remnants. Consequently, one concludes that the HR production mechanism is directly related to the dynamical IMF production process.

An important question to be addressed is what is the mechanism that inhibits fission and, hence, allows the frequent survival of heavy residues at high-energy losses or excitation energies, but does not allow such survival in less dissipative collisions. A possible explanation, offered in the literature, invokes a dynamical retardation of the fission process relative to neutron, LCP, and IMF evaporation [6–8]. IMF emission, which is enhanced at high excitation energies as the emission times decrease [37], is particularly effective in inhibiting fission. This is so because IMF emission is inherently associated with a significant reduction in atomic number, mass, and fissility of the emitters.

The trends seen in Figs. 19 and 20 suggest that it is indeed (dynamical) IMF production that is largely responsible for the survival of TLF residues. In Fig. 18, the HR energy spectrum (c) is measured in coincidence with at least three IMFs, a condition which is equivalent to the requirement of saturation of the thermal energy in the system. This requirement is seen to suppress the Gaussian-like component associated with TLF fission. This suppression is also clearly displayed

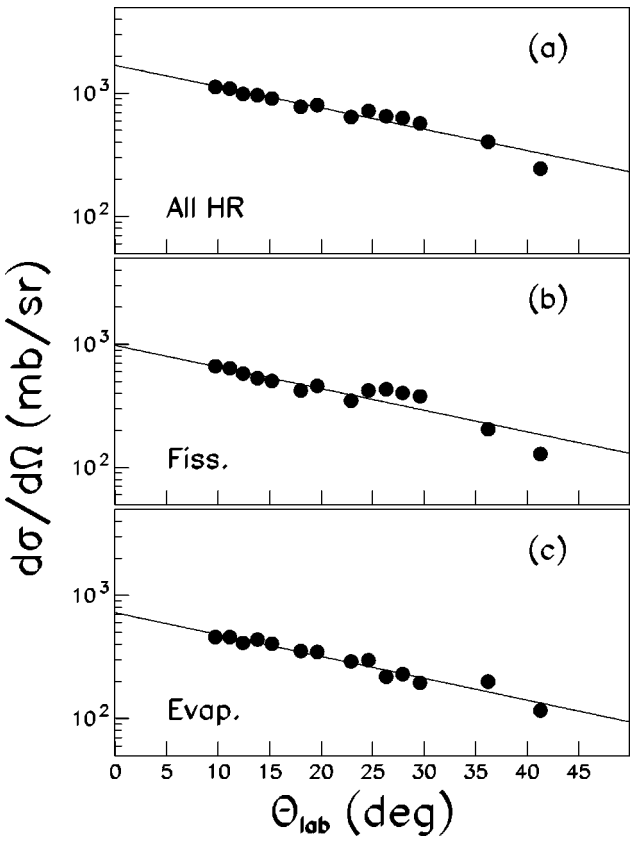

FIG. 25. Angular distributions of all heavy residues (top panel), TLF fission fragments (middle panel), and TLF evaporation residues (bottom panel).

in the two-dimensional plot, presented in Fig. 20, where the lower right panel shows HR yield plotted versus HR energy and charged-particle multiplicity, measured under the same conditions of $m_{IMF}>2$.

5. Fission versus evaporation competition

The measured laboratory angular distributions of heavy residues are presented in Fig. 25. The upper panel of this figure presents the inclusive distribution, while the middle and bottom panels represent evaporation and fission components, defined by the correlation between HR energy and charged-particle multiplicity (see Fig. 20). In all three cases, the yield increases exponentially with decreasing emission angle. The logarithmic slopes of the angular distributions are seen to be similar for evaporation and fission components, reflecting a common origin of these products—the primary TLF.

In order to determine the heavy-residue production cross section, their angular distributions were extrapolated by the straight lines shown in Fig. 25. An angular integration of these distributions yields a total cross section of $\sigma_{HR}\approx 2$ b and a ratio of the cross sections of the two components of $\sigma_{ER}/\sigma_{FF}\approx 0.7$. Similar results for the angular distributions and cross sections have been found [36,38,39] for other systems using different methods. The above total cross section should be regarded as a lower limit. Uncertainties, of the order of 30%, are due mostly to the high identification

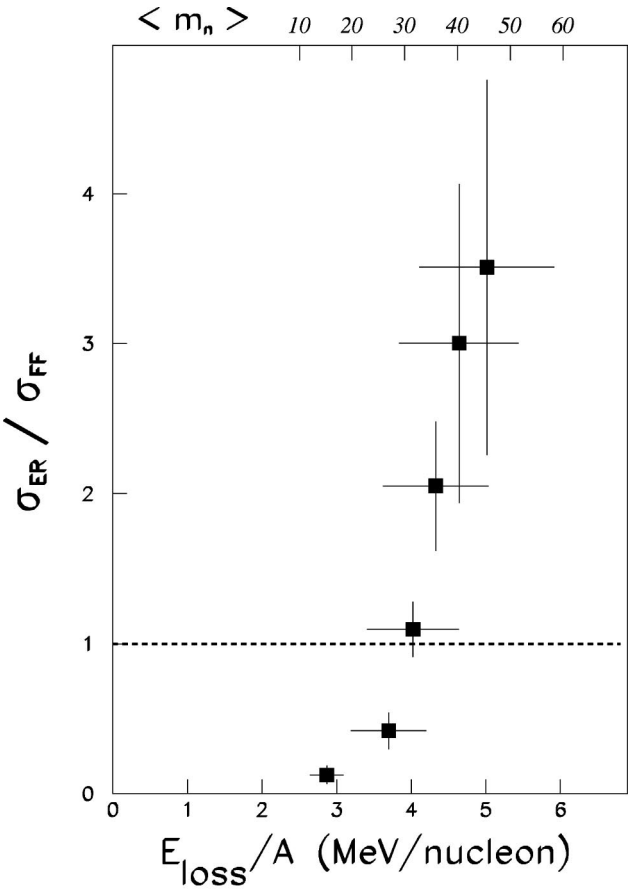

FIG. 26. Ratio of the production cross sections for TLF fission fragments and TLF evaporation residues as a function of kinetic-energy loss.

thresholds of heavy residues. In addition, the limited angular range of the HR detectors prevented detection of fragments emitted in quasielastic collisions at large angles.

As concluded above, both kinds of heavy residues, the TLF evaporation residues and the TLF fission fragments, originate from primary TLFs. Which mode of the TLF decay actually prevails appears to be decided by the statistical competition between particle emission and fission. The outcome of this competition is strongly affected by the size of the primary TLF (i.e., its fissility), and the latter is determined by the IMF production rate. The deduced competition between the fission and evaporation modes is illustrated in Fig. 26 as a function of the kinetic-energy loss. In this figure, the above competition is measured by the yield ratio σ_{ER}/σ_{FF}. The individual cross sections in this ratio were evaluated by integrating the angular distribution for each respective component. The different degrees of kinetic-energy dissipation were selected by setting gates on the joint distribution of multiplicities m_n and m_c and by deducing the corresponding kinetic-energy loss for each bin from the m_n-m_c correlations depicted in Fig. 6 and from the TLF-residue recoil velocity. The latter velocity was evaluated from an analysis of the LCP velocity spectra, assuming binary collision kinematics (see also the discussion of Fig. 15).

The energy-loss variable E_{loss}/A, where E_{loss} is the total energy dissipated and A is the initial number of nucleons in the entrance channel, can be viewed as an approximate measure of the excitation energy per nucleon of the system, $\epsilon^* \approx E_{loss}/A$. As the energy loss (excitation energy) increases, a steep increase is observed in the ratio σ_{ER}/σ_{FF}. Above $\epsilon^* = (3-4)$ MeV/nucleon of excitation energy, particle evaporation from the TLF competes successfully with TLF fission, demonstrating that TLF evaporation residues are produced in the most dissipative collisions and predominantly do not fission at high excitation energies. Note that Fig. 26 is valid only for the energy-loss domain covered by the data, in which a HR was identified at forward angles. These events do not include the elastic and quasielastic events for which the TLFs emerge with a low excitation energy, insufficient to overcome the fission barrier. For those events, one would expect a decreasing ratio σ_{ER}/σ_{FF} at very low energy losses. One notes that for a ^{197}Au nucleus, the fission barrier is ~ 16 MeV for zero angular momentum and it vanishes for an angular momentum $l \sim 82\hbar$.

IV. SUMMARY AND CONCLUSIONS

In the present work, results from an experiment on the ^{197}Au+ ^{86}Kr system at $E_{lab}/A = 35$ MeV were discussed, in which 4π measurements of neutrons and charged light and intermediate-mass products were performed, in coincidence with projectilelike or targetlike fragments.

The properties of projectilelike fragments were studied in detail. The reaction cross section was found to be $\sigma_R = (5.0 \pm 0.7)$ b, in good agreement with the systematics [29]. The deduced PLF deflection function was found consistent with a dissipative orbiting process, similar to the results [23] reported for the Bi+ Xe system at $E/A = 28$ MeV. The binary character of the collisions was found also reflected in the Galilei-invariant velocity distributions of the light-charged particles over the whole range of energy dissipation. It is found that even the most central collisions follow a dissipative scenario with PLFs and TLFs present in the exit channel in addition to IMFs. However, a complete damping of the available kinetic energy is observed only for events in the far tails of event distributions in all representations studied. In other words, it is not achieved for any class of events that could been selected by the selection criteria independent of the energy damping itself. The LCP properties indicate that, at most, 60% of the available kinetic energy is converted into thermal energy. The IMF properties indicate that their production process is dynamical and occurs at the interface of projectile and target. The IMF production mechanism appears to be an efficient channel that carries away a substantial part of the PLF-TLF relative energy.

An analysis of the exclusive yield of slow-moving residues measured in coincidence with PLFs, neutrons, light-charged particles, and intermediate-mass fragments showed that such residues are mostly produced in binary dissipative collisions. A lower limit for the heavy-residue cross section was found to be $\sigma_{HR} \sim 2$ b. The examination of the

associated Galilei-invariant distributions of the light-charged particles and the observed coincidence with massive PLFs proved that these residues are TLF remnants. Two classes of slow residues were found—TLF evaporation residues and TLF fission fragments. Significant differences in IMF multiplicities associated with these two classes are observed, indicating that IMF ''emission'' plays a decisive role in the survival of TLF evaporation residues. It is shown that above an excitation energy of 3–4 MeV/nucleon, the TLF fission mode fades away in favor of heavy-residue production, as the dynamical IMF production process reduces considerably the sizes and fissilities of the primary reaction fragments.

ACKNOWLEDGMENTS

The authors wish to express their appreciation of the hospitality extended to them at the MSU-NSCL and are grateful to the K1200 operations group. This work was supported by the U.S. Department of Energy under Grant Nos. DE-FG02-88ER-40414 (University of Rochester) and DE-FG02-87ER-40316 (Washington University at St. Louis).

[1] E. C. Pollaco *et al.*, Phys. Lett. **146B**, 29 (1984); M. Conjeaud *et al., ibid.* **159B**, 244 (1985).
[2] K. Aleklett *et al.*, Phys. Lett. B **236**, 404 (1990).
[3] J. F. Dempsey *et al.*, Phys. Rev. C **54**, 1710 (1996).
[4] W. Loveland *et al.*, Phys. Rev. C **41**, 973 (1990).
[5] E. Schwinn *et al.*, Nucl. Phys. **A568**, 169 (1994).
[6] D. Utley *et al.*, Phys. Rev. C **49**, R1737 (1994).
[7] E. C. Pollaco *et al.*, Nucl. Phys. **A583**, 441 (1995).
[8] R. Yanez *et al.*, Phys. Rev. C **52**, 203 (1995).
[9] A. A. Sonzogni *et al.*, Phys. Rev. C **53**, 243 (1996).
[10] R. Wada *et al.*, Phys. Rev. C **55**, 227 (1997).
[11] B. Lott *et al.*, in *Advances in Nuclear Dynamics*, edited by W. Bauer (World Scientific, Singapore, 1993), p. 62.
[12] J. Tõke *et al.*, Phys. Rev. Lett. **75**, 2920 (1995).
[13] J. Tõke *et al.*, in *Advances in Nuclear Dynamics*, edited by W. Bauer, W. Bauer, and G. Westfall (Plenum, New York, 1996), p. 49; J. Tõke *et al.*, Phys. Rev. Lett. **77**, 3514 (1996).
[14] C. P. Montoya *et al.*, Phys. Rev. Lett. **73**, 3070 (1994).
[15] W. Skulski *et al.*, Phys. Rev. C **53**, R2594 (1996).
[16] B. Djerroud *et al.*, in *Advances in Nuclear Dynamics* [13], p. 333.
[17] W. U. Schröder, DOE Report No. DOE/ER/79048-1, 1995.
[18] B. Quednau and D. Pade, Annual Progress Report No. DOE/ER/40414-2, 1989.
[19] J. Poitou and C. Signarbieux, Nucl. Instrum. Methods **114**, 11 (1974).
[20] J. Randrup, Nucl. Phys. **A307**, 319 (1978); **A327**, 490 (1979); **A383**, 468 (1982).
[21] R. J. Charity *et al.*, Nucl. Phys. **A483**, 371 (1988).
[22] B. Lott *et al.*, Phys. Rev. Lett. **68**, 3141 (1992).
[23] S. P. Baldwin, Ph.D thesis, University of Rochester, 1995; S. P. Baldwin *et al.*, Phys. Rev. Lett. **74**, 1299 (1995).
[24] W. U. Schröder *et al.*, Nucl. Sci. Res. Conf. Ser. **11**, 255 (1987).
[25] W. U. Schröder, Nucl. Phys. **A538**, 439c (1992).
[26] R. T. de Souza *et al.*, Phys. Rev. C **39**, 114 (1989).
[27] B. Borderie *et al.*, Phys. Lett. B **205**, 26 (1988).
[28] W. U. Schröder and J. R. Huizenga, *Treatise on Heavy-Ion Science* (Plenum, New York, 1984), Vol. 2.
[29] W. W. Wilcke *et al.*, At. Data Nucl. Data Tables **25**, 389 (1980).
[30] B. M. Quednau *et al.*, Phys. Lett. B **309**, 10 (1993).
[31] J. Wilczyński, Phys. Lett. **47B**, 124 (1973).
[32] J. F. LeColley *et al.*, Phys. Lett. B **325**, 317 (1994).
[33] J. Tõke and W. U. Schröder, Annu. Rev. Nucl. Part. Sci. **42**, 401 (1992).
[34] K. Aleklett *et al.*, Prog. Part. Nucl. Phys. **30**, 297 (1993); W. Loveland *et al.*, Phys. Lett. B **312**, 53 (1993).
[35] V. E. Viola, K. Kwiatkowski, and M. Walker, Phys. Rev. C **31**, 1550 (1985).
[36] E. Schwinn *et al.*, Nucl. Phys. **A568**, 169 (1994).
[37] Y. D. Kim *et al.*, Phys. Rev. Lett. **67**, 14 (1991).
[38] E. C. Pollaco *et al.*, Nucl. Phys. **A583**, 441 (1994).
[39] R. Yanez *et al.*, Phys. Rev. C **52**, 203 (1995).